Void Formation in Short-fiber Composites

A. NEEDLEMAN and S. R. NUTT
Division of Engineering, Brown University, Providence, RI 02912, USA

ABSTRACT

The effects of fiber spacing and fiber volume fraction on void nucleation in short-fiber composites are investigated through calculations based on a continuum model for interface decohesion. Using material parameters that simulate Al-SiC short-fiber composites, it is found that the stress and strain levels at which debonding occurs is strongly dependent on fiber spacing and volume fraction. In addition, fiber spacing also affects the mode of debonding at fiber ends. The results provide insight into the effects of controllable microstructural parameters on damage mechanisms that ultimately cause composite failure.

KEYWORDS

Void nucleation; damage; composite materials; finite element analysis.

INTRODUCTION

Aluminum alloys reinforced with short fibers of SiC exhibit substantial increases in yield strength, ultimate tensile strength, and elastic modulus, as well as improved resistance to creep and fatigue (Divecha *et al.*, 1981, Nieh, 1984 and Nair *et al.*, 1985). The observed property levels indicate a potential for weight reduction and improved performance characteristics in structural applications in the automotive and aerospace industries (McDaniels, 1985). However, Al-SiC composites also exhibit severely reduced ductility and low fracture toughness (Nair *et al.*, 1985). This behavior constitutes a major limitation for Al-SiC composites and prevents their employment in most of the intended applications.

One of the possible reasons for the premature failure of Al-SiC composites at low tensile strains involves void formation by interface debonding at fiber ends. In a previous study, voids at fiber ends in tensile fracture specimens have been observed and it was proposed that one cause of the low fracture toughness and ductility derived from the concentration of stress at fiber corners (Nutt and Duva, 1986). In the description of composite failure in (Nutt and Duva, 1986) localized plastic strains developed at low macroscopic stress levels because of the sharp corner profile at the fiber end, and cavitation ensued. More recently (Nutt and Needleman, 1987) a more complete analysis of the process of void nucleation at fiber ends has been carried out using a framework that permits quantitative predictions of the dependence of nucleation on matrix

material properties, interfacial cohesion characteristics and fiber volume fraction and geometry. Experimental observations by transmission electron microscopy of the deformed microstructure beneath tensile fracture surfaces showed distinct patterns of void evolution. These observations were compared with similar patterns of void formation predicted from model-based calculations using appropriate values for material parameters. The calculations indicated how the qualitative features of void nucleation, such as shape, size and location, depended on specific material parameters, such as interface strength and fiber geometry. The similarities between observed and predicted modes of void evolution were so pronounced that it was possible to quantify interface properties in the composite by comparisons between experimental observations and predictions based on model calculations.

The purpose of the present work is to examine the effects of parametric variations on the evolution of voids at fiber ends in Al-SiC composites under tensile loading. In particular, we examine the effects of variations in fiber volume fraction for a fixed fiber spacing and variations in fiber spacing for a fixed volume fraction. These effects are of great practical interest because of the local variations in fiber spacing and fiber volume fraction which inevitably occur in as-fabricated composites.

METHOD OF ANALYSIS

The analyses are based on the continuum model for interfacial decohesion presented in (Needleman, 1987). Within this framework, constitutive relations are specified independently for the matrix, the inclusions and the interface. The SiC inclusions are taken to be rigid and the Al matrix is modelled as a homogeneous, isotropic hardening, elastic- viscoplastic solid. Neither the residual stress distribution nor the nonhomogeneous matrix strength distribution that arise from prior thermo- mechanical processing are accounted for. The interfacial tractions are derived from a potential, which is taken to depend only on the displacement difference across the interface. In two dimensions, the interfacial tractions (force per unit initial area) are specified by (Needleman, 1987),

$$T_n = \frac{-27}{4}\sigma_{max}\left\{\left(\frac{u_n}{\delta}\right)\left[1-2\left(\frac{u_n}{\delta}\right)+\left(\frac{u_n}{\delta}\right)^2\right]+\alpha\left(\frac{u_t}{\delta}\right)^2\left[\left(\frac{u_n}{\delta}\right)-1\right]\right\} \tag{1}$$

$$T_t = \frac{-27}{4}\sigma_{max}\left\{\alpha\left(\frac{u_t}{\delta}\right)\left[1-2\left(\frac{u_n}{\delta}\right)+\left(\frac{u_n}{\delta}\right)^2\right]\right\} \tag{2}$$

for $u_n \leq \delta$ while $T_n \equiv T_t \equiv 0$ when $u_n > \delta$. For the axisymmetric configurations analyzed here, $\mathbf{n}$ and $\mathbf{t}$ refer to directions normal and tangential to the interface in the r−z plane of a polar coordinate system, and u_n and u_t are components of the displacement difference across the interface. The orientation of $\mathbf{n}$ is chosen so that positive u_n corresponds to increasing interfacial separation. From (1) and (2), the work of separation is

$$\phi_{sep} = 9\sigma_{max}\delta/16 \tag{3}$$

The interface is characterized by three parameters; the strength σ_{max}, the work of separation ϕ_{sep}, and the shear parameter α, which gives the ratio of shear stiffness to normal stiffness at $u_n = u_t = 0$. The values of σ_{max}, ϕ_{sep} and α are taken to be constant along the interface, although in principle they can be functions of position to account for variations in cohesion. The characteristic length δ is defined from (3) as $\delta = 16\phi_{sep}/9\sigma_{max}$. The value of δ does not represent the physical interface thickness, rather δ is a parameter characterizing the ductility of the process of interfacial separation (larger values of δ give rise to a more ductile mode of debonding). Since δ has dimensions of length, the predicted behavior depends on inclusion size at fixed volume fraction.

Figure 1 shows the normal traction, T_n, as a function of u_n with $u_t \equiv 0$. As can be seen in Fig. 1, the maximum interfacial stress, σ_{max}, is achieved at $u_n = \delta/3$ and complete separation occurs when $u_n = \delta$. In more general circumstances, where $u_t \not\equiv 0$, the curve of T_n versus u_n depends on the history of u_t. However, regardless of the history of u_t, both T_n and T_t vanish at $u_n = \delta$ and, since there is an interfacial potential, the work of separation is given by (3). The interfacial constitutive relation used here posses the convenient feature that the traction vanishes at a finite separation so that there is a well defined decohesion point. However, atomistic calculations of interfacial separation, (Rose *et al.*, 1981), suggest an exponential form, which can readily be incorporated into the formulation (Needleman, 1988).

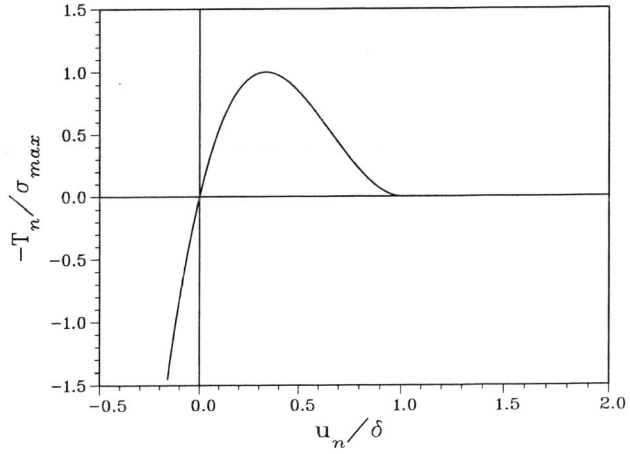

Fig. 1. Normal traction across the interface as a function of u_n with $u_t \equiv 0$.

The finite element analysis is based on a convected coordinate Lagrangian formulation of the field equations with the initial unstressed state taken as reference. All field quantities are considered to be functions of convected coordinates, x^i, which serve as particle labels, and time t. Attention is confined to quasi-static deformations and, with body forces neglected, the principal of virtual work is written as

$$\int_V \tau^{ij}\delta E_{ij}dV + \int_{S_{int}} \delta\phi dS = \int_{S_{ext}} T^i \delta u_i dS \tag{4}$$

Here, τ^{ij} are the contravariant components of Kirchhoff stress ($\boldsymbol{\tau} = J\boldsymbol{\sigma}$, with $\boldsymbol{\sigma}$ the Cauchy stress) on the deformed convected coordinate net, V, S_{ext} and S_{int} are the total volume (inclusion plus matrix), external surface and interfacial surface, respectively, of the body in the reference configuration, and

$$T^i = (\tau^{ij} + \tau^{kj}u^i_{,k})\nu_j \tag{5}$$

$$E_{ij} = \frac{1}{2}(u_{i,j} + u_{j,i} + u^k_{,i}u_{k,j}) \tag{6}$$

where $\boldsymbol{\nu}$ is the surface normal in the reference configuration, u_j are the components of the displacement vector on base vectors in the reference configuration and $()_{,i}$ denotes covariant differentiation in the reference frame.

The matrix material is characterized as an elastic-viscoplastic isotropically hardening solid. The total rate of deformation, $\mathbf{D}$, is written as the sum of an elastic part, $\mathbf{D}^e$, and a plastic part $\mathbf{D}^p$, with

$$\mathbf{D}^e = \frac{1+\nu}{E}\hat{\boldsymbol{\tau}} - \frac{\nu}{E}(\hat{\boldsymbol{\tau}} : \mathbf{I})\mathbf{I} \tag{7}$$

$$\mathbf{D}^p = \frac{3\dot{\bar{\epsilon}}}{2\bar{\sigma}}\boldsymbol{\tau}' \tag{8}$$

where $\hat{\boldsymbol{\tau}}$ is the Jaumann rate of Kirchhoff stress, $\mathbf{I}$ is the identity tensor, $\hat{\boldsymbol{\tau}} : \mathbf{I}$ is the trace of $\hat{\boldsymbol{\tau}}$, $\dot{\bar{\epsilon}}$ is the effective plastic strain rate, E is Young's modulus, ν is Poisson's ratio and

$$\boldsymbol{\tau}' = \boldsymbol{\tau} - \sigma_m \mathbf{I} \quad \sigma_m = \frac{1}{3}(\boldsymbol{\tau} : \mathbf{I}) \quad \bar{\sigma}^2 = \frac{3}{2}\boldsymbol{\tau}' : \boldsymbol{\tau}' \tag{9}$$

$$\dot{\bar{\epsilon}} = \dot{\epsilon}_0[\bar{\sigma}/g(\bar{\epsilon})]^{1/m} \ , \ g(\bar{\epsilon}) = \sigma_0(\bar{\epsilon}/\epsilon_0 + 1)^N \ , \ \epsilon_0 = \sigma_0/E \tag{10}$$

Here, $\bar{\epsilon} = \int \dot{\bar{\epsilon}} dt$ and the function $g(\bar{\epsilon})$ represents the effective stress versus effective strain response in a tensile test carried out at a strain-rate such that $\dot{\bar{\epsilon}} = \dot{\epsilon}_0$. Also, σ_0 is a reference strength and N and m are the strain hardening exponent and strain rate hardening exponent, respectively.

The inelastic uniaxial tensile response of the Al matrix are specified by $\sigma_0 = 332$MPa, $E = 74$GPa and $N = 0.1$. These values are chosen to be representative of the average tensile properties reported for the P/M 6061 Al-T6 matrix material (Nardone and Prewo, 1986). Poisson's ratio, ν, is 0.3 and the strain rate hardening exponent, m, is taken as 0.004, which corresponds to slightly less than a 1% increase in strength level per order of magnitude increase in strain rate.

The specific boundary value problem analyzed is one simulating a three dimensional periodic array of circular cylindrical inclusions subject to a tensile stress parallel to the fiber axes. Each cell in the periodic array is approximated by a circular cylinder and is required to remain a circular cylinder throughout the deformation history in order to represent the constraint imposed by the surrounding material. Symmetry about the midplane of the cell is also enforced. Using a cylindrical coordinate system with radial coordinate x^1, circumferential angle x^2 and axial coordinate x^3, the boundary conditions for the axisymmetric region analyzed numerically are

$$\dot{u}^3 = 0 \ , \ \dot{T}^1 = 0 \ , \ \dot{T}^2 = 0 \ , \text{ on } \ x^3 = 0 \tag{11}$$

$$\dot{u}^3 = \dot{U}_3 = \dot{\epsilon}_{ave}(b_0 + U_3) \ , \ \dot{T}^1 = 0 \ , \ \dot{T}^2 = 0 \ , \text{ on } \ x^3 = b_0 \tag{12}$$

$$\dot{u}^1 = \dot{U}_1 \ , \ \dot{T}^3 = 0 \ , \ \dot{T}^2 = 0 \ , \text{ on } \ x^1 = R_0 \tag{13}$$

Here, $(\dot{}) = \partial()/\partial t$ and $\dot{\epsilon}_{ave}$ is a prescribed constant while $\dot{U}_1$ is determined from the condition that the average macroscopic true stress acting on the cell side vanishes. The axial tensile strain rate, $\dot{\epsilon}_{ave}$, is prescribed equal to the material reference strain rate, $\dot{\epsilon}_0$ in (12), but with the very low strain rate hardening exponent characterizing the Al matrix, rate effects play a negligible role.

NUMERICAL RESULTS

In the calculations carried out here, the material properties and interface characteristics remain fixed; only the fiber volume fraction and spacing are varied. The material properties are given above, the interfacial strength, σ_{max}, is specified as $\sigma_{max} = 5\sigma_0 = 1660$MPa and the remaining interface properties are given by taking the characteristic length, δ, as 0.01 times the inclusion diameter and the shear parameter $\alpha = 1$ in (1) and (2). Furthermore, the ratio of fiber length to fiber diameter is fixed at 4.

Figure 2 shows curves of average axial stress, σ_{ave}, versus average axial strain, $\epsilon_{ave} = \ln(1 + U_3/b_0)$, for fiber volume fractions of 10%, 20% and 30%. In each case the cell aspect ratio is taken to be 4. Denoting the fiber radius by r_0, these three volume fractions have ratios of fiber radius to cell radius of $r_0/R_0 = 0.463$, $r_0/R_0 = 0.588$ and $r_0/R_0 = 0.667$, respectively. The abrupt stress drop is associated with the normal traction near the fiber corner passing through the maximum and the onset of decohesion. The decohesion initiation strain decreases with increasing fiber volume fraction. The stress drop increases with increasing fiber volume fraction. It should be noted that this stress drop is a local one for the neighborhood of a single debonding fiber. The overall situation modelled is for a regular array of fibers each of which is deforming identically so that if the curves in Fig. 2 are regarded as overall response curves, they correspond to all fibers debonding simultaneously. Furthermore, due to the symmetry imposed in the calculations voids initiate simultaneously at the top and bottom of each fiber. Figure 3 shows deformed meshes at the last stage of deformation for each of the calculations in Fig. 2. The region shown is the quadrant analyzed numerically and the rigid fiber is indicated by the shaded region.

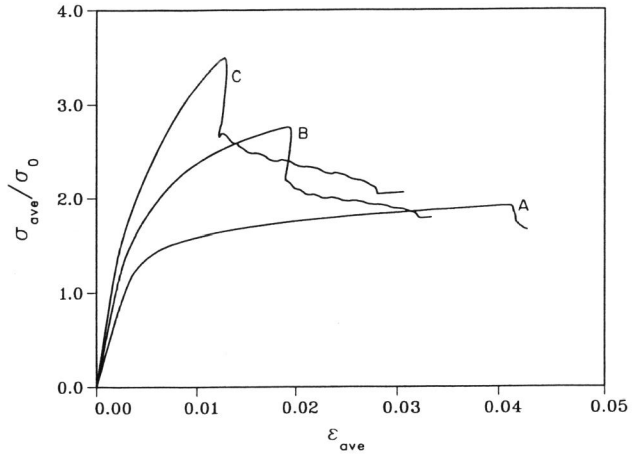

Fig. 2. Curves of average axial true stress versus logarithmic axial strain for (A) 10% fiber volume fraction (B) 20% fiber volume fraction and (C) 30% fiber volume fraction. In each case, the cell aspect ratio equals the fiber aspect ratio which is 4.

The effect of fiber spacing at a fixed fiber volume fraction of 20% is shown in Fig. 4. The three spacings considered have ratios of fiber radius to cell radius of $r_0/R_0 = 0.463$, $r_0/R_0 = 0.588$ and $r_0/R_0 = 0.667$. Curve B, $r_0/R_0 = 0.588$, is repeated from Fig. 2. The fiber spacings for the other two cases can be seen in Figs. 5 and 6. The elastic stiffness increases as the end-to-end fiber spacing decreases. The two cases having well separated fiber ends have a very similar overall behavior. When the end-to-end spacing is very close, debonding initiates along the centerline, rather than at the fiber corner, and at a comparatively small overall strain. There is an abrupt load drop and then the stress decreases gradually as the void grows. As can be seen in Fig. 4, although the stress-strain response prior to debonding is sensitive to the fiber spacing, the stress levels after some void growth are not very different.

Figure 5 shows contours of constant Mises equivalent plastic strain, $\bar{\epsilon}$, in the deformed configu-

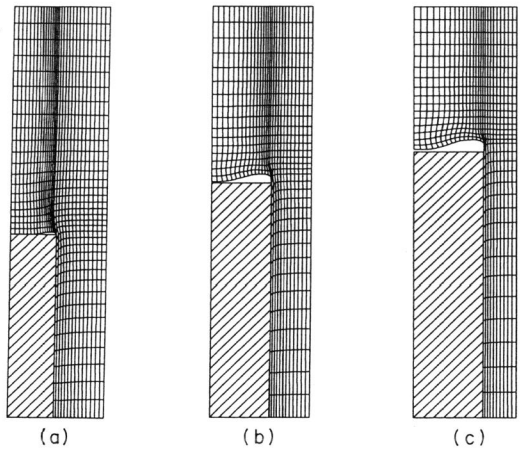

Fig. 3. Deformed finite element meshes for the quadrant analyzed numerically for (a) 20% fiber volume fraction, at $\epsilon_{ave} = 0.0427$, (b) 20% fiber volume fraction, at $\epsilon_{ave} = 0.0334$ and (c) 30% fiber volume fraction, at $\epsilon_{ave} = 0.0308$. The tension axis is vertical and the fiber is shaded.

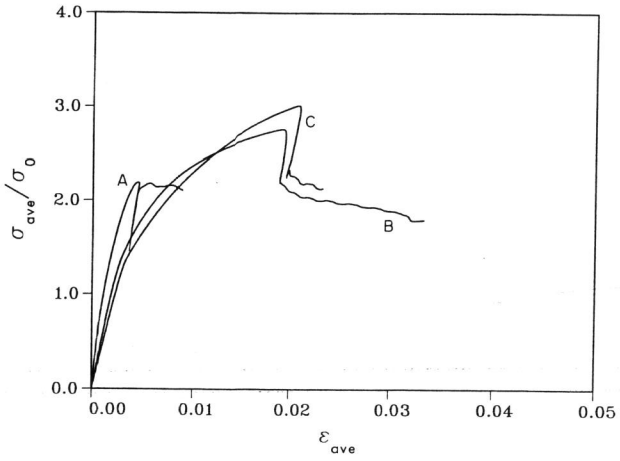

Fig. 4. Curves of average axial true stress versus logarithmic axial strain for 20% fiber volume fraction (A) $r_0/R_0 = 0.463$ (B) $r_0/R_0 = 0.588$ and (C) $r_0/R_0 = 0.667$.

ration for the two extreme fiber spacing cases in Fig. 4. The present results show a transition in mode of debonding with decreasing end-to-end spacing. When fiber ends are well separated, debonding initiates at the corners. For sufficiently close fibers, and how close that is undoubtedly depends on material properties and interface characteristics, debonding initiates along the

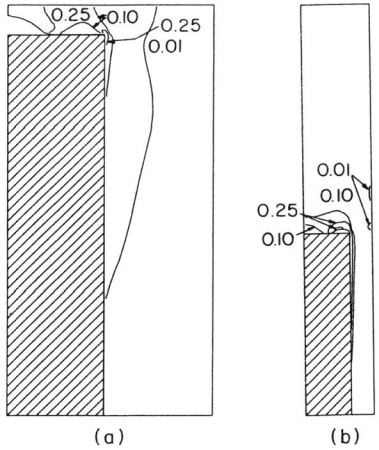

Fig. 5. Contours of constant plastic strain, $\bar{\epsilon}$, in the deformed configuration of the quadrant analyzed numerically for (a) $r_0/R_0 = 0.463$ at $\epsilon_{ave} = 0.00893$ and (b) $r_0/R_0 = 0.667$ at $\epsilon_{ave} = 0.0233$. The tension axis is vertical and the fiber is shaded.

centerline. At some transition distance nearly simultaneous debonding is possible. In fact, case B was also analyzed in (Nutt and Needleman, 1987) but using a different finite element mesh. Very good agreement is found through initial debonding. However, in (Nutt and Needleman, 1987) debonding at the center followed debonding at the corner whereas here we only find debonding at the corner. This spacing is one for which the competition between corner and center debonding is very close and mesh design can influence the calculated mode of debonding. The shift in debonding mode arises from the high hydrostatic tension that develops at the center of the fiber end when the end-to-end spacing is small. This is illustrated in Fig. 6, where contours of constant mean normal stress are plotted for $r_0/R_0 = 0.463$ and $r_0/R_0 = 0.667$ prior to debonding.

DISCUSSION

We have examined the effects of fiber volume fraction and fiber spacing on the formation of voids at fiber ends in composites subjected to tensile loading. Our calculations show how the size, shape, and location of voids depend on the microstructural parameters of fiber volume fraction and fiber spacing. Furthermore, the results of the calculations provide quantitative indications of the effects of these parameters on the levels of stress and strain at which debonding occurs, as shown in Figures 2 and 4. Within the composite, local fiber spacings (and volume fractions) vary substantially from fiber spacings averaged over the bulk composite because the distribution of submicron constituents is difficult to control (Nardone and Prewo, 1986). Nonuniform distribution of the reinforcing phase contributes to the localization of plastic strain and the premature onset of failure processes at low macroscopic strains (Nardone and Prewo, 1986). The extremely low levels of toughness and ductility reported for Al-SiC composites (Divecha *et al.*, 1981 and Nair *et al.*, 1985) and the fact that voids in tensile fracture specimens are observed only near the fracture surface (Nutt and Needleman, 1987) suggest that composite failure is controlled by the onset of damage mechanisms such as void nucleation. Our results indicate how void formation at fiber ends is affected by fiber volume concentration and spacing.

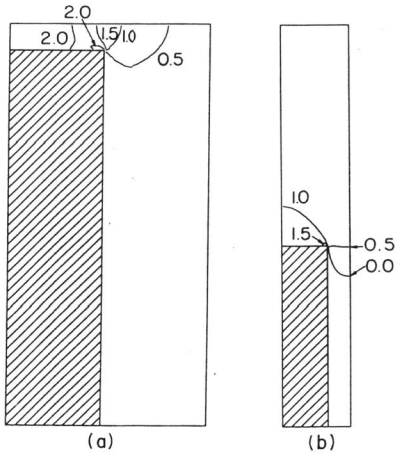

Fig. 6. Contours of mean normal stress, σ_m/σ_0, in the deformed configuration of the quadrant analyzed numerically for (a) $r_0/R_0 = 0.463$ at $\epsilon_{ave} = 0.00152$ and (b) $r_0/R_0 = 0.667$ at $\epsilon_{ave} = 0.00416$. The tension axis is vertical and the fiber is shaded.

ACKNOWLEDGEMENTS

The work of AN was supported by ONR contract number N00014-86-K-0262 and the work of SRN was supported by ONR contract number N00014-86-K-0125. This support is gratefully acknowledged.

REFERENCES

Divecha, A.P., S.G. Fishman, and S.D. Demarkar (1981). Silicon carbide reinforced aluminum-a formable composite. *J. Metals*, **33**, 12-17.

McDanels, D.L. (1985). Analysis of stress-strain, fracture and ductility behavior of aluminum matrix composites containing discontinuous silicon carbide reinforcement. *Metall. Trans.*, **16A**, 1105-1115.

Nair, S.V., J.K Tien, and R.C. Bates, (1985). Si-C reinforced aluminum metal matrix composites. *Int. Met. Rev.*, **30**, 275-290.

Nardone, V.C. and K.M. Prewo (1986). On the strength of discontinuous silicon carbide reinforced aluminum composites. *Scripta Metall.*, **20**, 43-48.

Needleman, A. (1987). A continuum model for void nucleation by inclusion debonding. *J. Appl. Mech.*, **54**, 525-531.

Needleman, A. (1988). An analysis of decohesion along an imperfect interface. *Int. J. Frac.*, to be published.

Nieh, T.G. (1984). Creep rupture of a silicon carbide reinforced aluminum composite. *Metall. Trans.*, **15A**, 139-146.

Nutt, S.R. and J.M. Duva (1986). A failure mechanism in Al-SiC composites. *Scripta Metall.* **20**, 1055-1058.

Nutt, S.R. and A. Needleman (1987). Void nucleation at fiber ends in Al-SiC composites. *Scripta Metall.*, **21**, 705-710.

Rose, J.H., J. Ferrante and J.R. Smith (1981). Universal binding energy curves for metals and bimetallic interfaces. *Phys. Rev. Lett.*, **47**, 675-678.